

# Atmospheric Ice Particle Shape Estimates from Polarimetric Radar Measurements and In Situ Observations

SERGEY Y. MATROSOV

*Cooperative Institute for Research in Environmental Sciences, University of Colorado Boulder,  
and NOAA/Earth System Research Laboratory, Boulder, Colorado*

CARL G. SCHMITT

*National Center for Atmospheric Research, Boulder, Colorado*

MAXIMILIAN MAAHN AND GIJS DE BOER

*Cooperative Institute for Research in Environmental Sciences, University of Colorado Boulder,  
and NOAA/Earth System Research Laboratory, Boulder, Colorado*

(Manuscript received 16 June 2017, in final form 15 September 2017)

## ABSTRACT

A remote sensing approach to retrieve the degree of nonsphericity of ice hydrometeors using scanning polarimetric Ka-band radar measurements from a U.S. Department of Energy Atmospheric Radiation Measurement (ARM) Program cloud radar operated in an alternate transmission–simultaneous reception mode is introduced. Nonsphericity is characterized by aspect ratios representing the ratios of particle minor-to-major dimensions. The approach is based on the use of a circular depolarization ratio (CDR) proxy reconstructed from differential reflectivity  $Z_{DR}$  and copolar correlation coefficient  $\rho_{mv}$  linear polarization measurements. Essentially combining information contained in  $Z_{DR}$  and  $\rho_{mv}$ , CDR-based retrievals of aspect ratios are fairly insensitive to hydrometeor orientation if measurements are performed at elevation angles of around  $40^{\circ}$ – $50^{\circ}$ . The suggested approach is applied to data collected using the third ARM Mobile Facility (AMF3), deployed to Oliktok Point, Alaska. Aspect ratio retrievals were also performed using  $Z_{DR}$  measurements that are more strongly (compared to CDR) influenced by hydrometeor orientation. The results of radar-based retrievals are compared with in situ measurements from the tethered balloon system (TBS)-based video ice particle sampler and the ground-based multiangle snowflake camera. The observed ice hydrometeors were predominantly irregular-shaped ice crystals and aggregates, with aspect ratios varying between approximately 0.3 and 0.8. The retrievals assume that particle bulk density influencing (besides the particle shape) observed polarimetric variables can be deduced from the estimates of particle characteristic size. Uncertainties of CDR-based aspect ratio retrievals are estimated at about 0.1–0.15. Given these uncertainties, radar-based retrievals generally agreed with in situ measurements. The advantages of using the CDR proxy compared to the linear depolarization ratio are discussed.

## 1. Introduction

Ice particles in atmospheric clouds and precipitation have a great variety of shapes and types (i.e., habits). Particle habits influence important microphysical (e.g., crystal growth, evaporation, and sedimentation rates) and radiative (e.g., longwave and shortwave extinction, and scattering) processes. Therefore, understanding and quantifying particle habits are critical for refining regional and global climate models (e.g., Kokhanovsky

and Macke 1999) and improving quantitative precipitation estimation (QPE) of snowfall (e.g., Ryzhkov et al. 2017). In situ data indicate that most atmospheric ice hydrometeors in the Arctic are frequently of irregular shape (e.g., Korolev et al. 1999; Korolev and Isaac 2003; Hogan et al. 2012).

One simple quantitative characteristic of irregular ice particles is their aspect ratio (Korolev and Isaac 2003), which is usually defined as the ratio of particle minor and major dimensions with the minor axis defined as perpendicular to the major axis. The particle aspect ratio is also used as a quantitative parameter in atmospheric modeling studies (e.g., Sheridan et al. 2009; Avramov

---

*Corresponding author:* Sergey Y. Matrosov, sergey.matrosov@noaa.gov

and Harrington 2010; Jensen et al. 2017). The simplest shape that accounts for particle general nonsphericity is the spheroidal shape representing an ellipsoid, where two out of three axes are of the same length. The oblate spheroidal shape is widely used to describe raindrops and has been used for describing ice particles in radar studies (e.g., Matrosov et al. 2001, 2012; Melnikov and Straka 2013; Myagkov et al. 2016a,b) at different frequency bands. This simple shape assumption satisfactorily describes observed vertically pointing radar depolarization ratios and reflectivity enhancements for different particle habits (Matrosov 2015). Pristine solid ice density hexagonal prism models have also been used for retrieving particle shapes (e.g., Melnikov 2017). In situ measurements, however, indicate that such pristine habits describe only a very small percentage ( $\sim 3\%$ ) of observed ice particles (e.g., Korolev et al. 1999). Because of the importance of particle shapes in climate modeling and QPE applications, it is desirable that remote sensing measurements provide information on particle aspect ratios.

Polarimetric radar measurements provide a means for estimation of ice particle aspect ratios. The first polarimetric cloud radars (e.g., Kropfli et al. 1990) were designed to measure a single polarimetric variable: depolarization ratio (DR), defined as the ratio of radar returns on two orthogonal polarizations when signals on one of these polarizations are transmitted. It has been shown (Matrosov et al. 2001) that the slant- $45^\circ$  linear depolarization ratio (SLDR) and circular depolarization ratio (CDR) are best suited for particle shape estimation, since these polarimetric variables (while sensitive to hydrometeor shape and density) are relatively insensitive to particle orientation. When particles are generally oriented with their larger dimensions in the horizontal plane, CDR is very close to SLDR. When horizontal (or vertical) polarization signals are transmitted, conventional linear depolarization ratio (LDR) measurements are less favorable for estimation of particle shape as a result of high sensitivity to particle orientation and weaker cross-polarized radar signals, resulting in the fact that LDR is usually available only at close radar ranges.

Over the last 15 years or so, operational and research meteorological radars that simultaneously transmit and simultaneously receive (STSR) horizontally and vertically polarized signals (Doviak et al. 2000) have become common. This mode of operation, which is sometimes also called the hybrid mode, provides measurements of several polarimetric variables, including differential reflectivity  $Z_{DR}$  and copolar correlation coefficient  $\rho_{hv}$  between backscatter amplitudes on horizontal and vertical polarizations. It was shown (e.g., Melnikov and

Straka 2013; Myagkov et al. 2016a) that a combined analysis of  $Z_{DR}$  and  $\rho_{hv}$  yields information on particle habits for a given assumption of the shape model (e.g., spheroidal shapes). These two variables can be used to calculate a depolarization ratio proxy, which is close to CDR if the phase shift between horizontally and vertically polarized signals is close to  $90^\circ$  (Ryzhkov et al. 2017). The polarization cross coupling, which exists in STSR  $Z_{DR}$  measurements and depends on the transmission phase difference between horizontally and vertically polarized signals, however, contributes to uncertainties in particle habit retrievals.

Several observational facilities of the U.S. Department of Energy (DOE) Atmospheric Radiation Measurement (ARM) Program have been recently equipped with scanning ARM cloud radars (SACRs) operating at Ka ( $\sim 35$  GHz) and W ( $\sim 94$  GHz) bands (Kollias et al. 2014). Newer versions of these radars, including one which is a part of the third ARM Mobile Facility (AMF3) deployed to Oliktok Point, Alaska ( $70.495^\circ\text{N}$ ,  $149.886^\circ\text{W}$ ), transmit horizontally and vertically polarized signals alternatively, thus alleviating cross-coupling effects. Differential phase,  $\rho_{hv}$ , and LDR measurements are directly available from these radars.

The objectives of this study are to evaluate the use of measurements from these new SACRs to estimate aspect ratios of irregular/aggregate ice particles and to compare radar-based retrievals with collocated observations from two in situ instruments: the ground-based multiangle snowflake camera (MASC; Garrett et al. 2012) and the balloonborne video ice particle sampler (VIPS; Schmitt et al. 2013).

## 2. Theoretical modeling of polarimetric radar variables for ice hydrometeors

It has been shown previously (e.g., Matrosov et al. 2001, 2012; Reinking et al. 2002) that pristine ice particles (e.g., plates, dendrites, columns, needles) can be successfully identified and that more complex planar-type ice particles can be distinguished from the columnar-type particles using the radar elevation angle dependences of depolarization ratios. While planar hydrometeors (e.g., dendrites, plates, and their aggregates) exhibit the smallest depolarization at vertical viewing and increasing depolarization ratios as viewing goes to slant, columnar crystals are characterized by depolarization ratio values that do not show significant elevation angle dependence but are higher than the minimum depolarization ratio ( $DR_{\min}$ ), which depends on radar hardware.

A spheroidal shape (i.e., oblate spheroidal shape for planar-type particles and prolate spheroidal shape for columnar-type particles) assuming a homogeneous

ice–air mixture provides a convenient description of irregular ice particles whose nonsphericity is characterized by a simple aspect ratio parameter. However, modeling studies of ice particle scattering properties at high frequencies with complex shapes indicate that the spheroidal model has limitations when particle sizes are similar and (especially) large compared to the radar wavelength (Leinonen et al. 2012, and references therein), so more robust computational approaches such as the discrete dipole approximation (DDA) are preferable. Given this, further polarimetric variable modeling in this study was performed for the Ka-band SACR frequency ( $\sim 35$  GHz). At this frequency, limitations of the T-matrix calculations for the spheroidal shape model are much less pronounced compared to the W band ( $\sim 94$  GHz), especially for variables integrated over the size distributions of irregular-shaped particles having aspect ratios larger than pristine crystals.

Close correspondence between spheroidal shape model CDR and SLDR calculations and observed depolarization signatures for different ice particle habits at Ka band (Matrosov et al. 2001; Reinking et al. 2002) serves as a further justification for the use of this shape model. The spheroidal shape is also often used in cloud microphysical parameterization schemes (e.g., Sheridan et al. 2009; Jensen et al. 2017). Additionally, unlike some other simple approaches applied for larger particle reflectivity calculations (e.g., Hogan and Westbrook 2014), use of the T-matrix approach for spheroidal shapes is convenient for calculating polarimetric variables. Modeling of radar polarimetric variables using the T-matrix approach (e.g., Mishchenko and Travis 1994) with accounting for the radar hardware polarimetric “cross talk” is described by Matrosov (2015). This approach was used in this study.

Gamma-function particle size distribution (PSD) assumption is customary used in modeling, since such a PSD shape generally describes well microphysical observations (e.g., Kosarev and Mazin 1991). Relative radar variables (e.g., depolarization ratios and differential reflectivity) are insensitive to the PSD intercept parameter, and for a given PSD shape these variables depend on median volume particle size  $D_{mv}$ , which is a characteristic particle size describing the entire PSD. For a fixed particle aspect ratio, this has two reasons: (i) a change of particle density with size and (ii) non-Rayleigh scattering for larger particles. The density effect is generally stronger than the non-Rayleigh scattering effect. Hereafter, individual particle density is understood as the ratio of particle mass and spheroidal particle volume; individual particle size  $D$  is usually defined as the particle’s major dimension.

Because of aerodynamic forcing, nonspherical particles tend to orient with their major dimensions in a horizontal

plane. For pristine crystals, characterized by small aspect ratios  $r$ , standard deviations around this preferential orientation are small (Matrosov et al. 2005). However, particles with larger values of  $r$  can be oriented more randomly (Garrett et al. 2015). To assess the orientation effect, polarimetric variable modeling was performed for different angular standard deviation ( $\sigma_\theta$ ) values (assuming a Gaussian distribution) from horizontal.

Figure 1 shows results of modeling different Ka-band polarimetric radar variables for planar-type (i.e., oblate) particles assuming different  $r$ ,  $D_{mv}$ ,  $\sigma_\theta$ , and the first-order gamma-function PSD. To illustrate the influence of particle mass–size ( $m$ – $D$ ) relations, three different assumptions for such relation were used. The  $m$ – $D$  relation analyzed by Brown and Francis (1995, hereafter BF95) ( $m = 0.0029 D^{1.9}$ , cgs units) has been widely used in the cloud microphysical community and was shown to closely approximate the direct bulk ice water content (IWC) measurements from several experiments (Heymsfield et al. 2016). A correction for the fact that BF95 was initially suggested in terms of the mean particle size  $D_{mean}$  was introduced as in Hogan et al. (2012). When applied to spheroidal particles, the Matrosov (2007, hereafter M07)  $m$ – $D$  relation ( $m = 0.003 D^2$  for  $D \leq 0.2$ ,  $m = 0.0067 D^{2.5}$  for  $0.2 < D \leq 2$ , cgs units) provides a continuous transition from particle densities typical for smaller cloud particles to those measured for larger snowflakes as documented by Magono and Nakamura (1965). The Heymsfield et al. (2013, hereafter H13) relation ( $m = 0.0052 D^{2.1}$ , cgs units) is based on a large dataset using the bulk counterflow virtual impactor with 2D microphysical probes. For a given particle size, this relation provides mass results within 12% of median relations obtained by von Lerber et al. (2017) for falling snow particles, under conditions when the supercooled liquid water path is less than  $320 \text{ g m}^{-2}$ .

Model calculation results presented in Fig. 1 assume that  $DR_{min} = -26.5$  dB. Accounting for actual  $DR_{min}$  values was performed as in Matrosov (2015), and it is essential for modeling realistic depolarization ratios for a given radar system. A  $-26.5$ -dB value for the Ka-band AMF3 SACR was found using radar measurements from nearly spherical drizzle-type drop scatterers. An example of such measurements is shown in Fig. 2.

Although SACR depolarization measurements include only LDR, other types of depolarization ratios are shown in Fig. 1. In addition to “true” depolarization ratios, which could be directly measured when the radar transmits circular or linear polarized signals (i.e., CDR or LDR), Fig. 1 also shows results for the proxy of CDR measurements  $CDR_p$  that can be obtained from measurements in the traditional horizontal–vertical (h–v) polarization base SACR measurements. Jameson (1987)

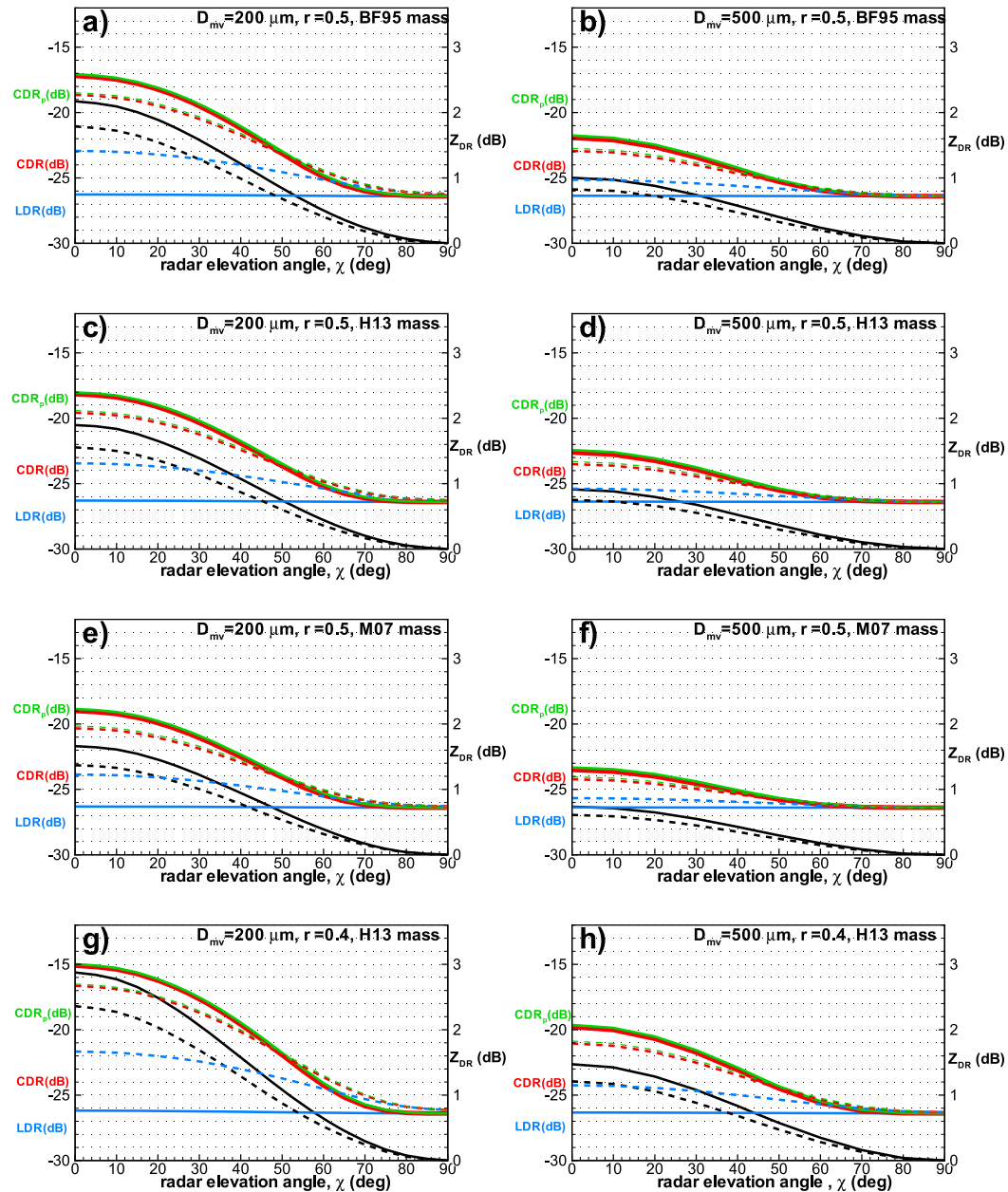


FIG. 1. Ka-band modeled elevation angle dependencies of  $Z_{DR}$  (black),  $CDR_p$  (green),  $CDR$  (red), and  $LDR$  (violet) for planar-type ice particles for different values of  $r$ ,  $D_{mv}$ , and  $m$ - $D$  assumptions. Shown are  $\sigma_\theta = 3^\circ$  (solid lines) and  $\sigma_\theta = 20^\circ$  (dashed lines) from particle orientation with major dimensions in the horizontal plane.

showed that circular depolarization ratios in linear units,  $C_{dr}$  [ $CDR(\text{dB}) = 10 \log_{10}(C_{dr})$ ], is related to the polarimetric variables in the traditional linear base as

$$C_{dr} = (Z_{dr} + 1 + 4 Z_{dr} L_{dr} - 2 Z_{dr}^{0.5} \rho_{hv}) / (Z_{dr} + 1 + 2 Z_{dr}^{0.5} \rho_{hv}), \quad (1)$$

where  $Z_{dr}$  and  $L_{dr}$  are differential reflectivity and the linear depolarization ratio in the h-v polarization base

in the linear units, respectively [i.e.,  $Z_{DR}(\text{dB}) = 10 \log_{10}(Z_{dr})$  and  $LDR(\text{dB}) = 10 \log_{10}(L_{dr})$ ], and  $\rho_{hv}$  is the copolar correlation coefficient. SACR cross-polar return signals are often below a reliable signal-to-noise threshold and thus are not usable, so  $LDR$  measurements are often unavailable. Besides,  $LDR$  values are generally very small ( $< -20$  dB) even when they can be measured. The corresponding circular depolarization ratio proxies from (1) are further

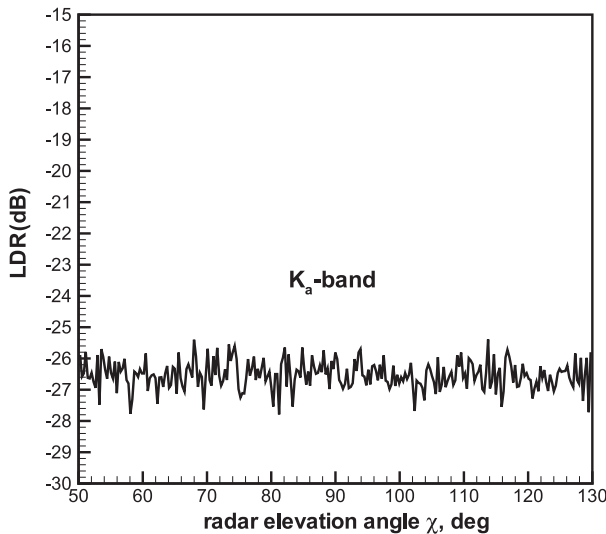


FIG. 2. Oliktok SACR LDR measurements during drizzle-like rain on 21 Jun 2016.

expressed in logarithmic units and are denoted as  $CDR_p = 10 \log_{10}(C_{dr})$ .

Earlier estimators similar to (1), when neglecting the  $L_{dr}$  term, were applied for the radars operating in the STSR measurement mode (Melnikov and Matrosov 2013; Ryzhkov et al. 2017), which has some  $Z_{dr}$  polarimetric coupling. Calculating the CDR proxy from STSR radar measurements generally requires tuning the transmission phase shift to get a better approximation of CDR (Ryzhkov et al. 2017). Because of its fully polarimetric alternate h–v transmission configuration, this is not an issue when using the SACR linear polarization variables to calculate  $CDR_p$  as in (1). Differential attenuation effects are neglected in (1), since attenuation in the ice phase is very minor and signal attenuation from supercooled liquid drops is not expected to produce differential effects because such drops in mixed-phase clouds and precipitation are generally small and nearly spherical.

While being a depolarization ratio proxy,  $CDR_p$  has several important practical advantages compared to “true” CDR. One such advantage is the absence of propagation effects (Ryzhkov et al. 2017), which otherwise cause an increase of observed CDR compared to its intrinsic values and thus hinder interpretation of circular depolarization measurements. Another important advantage is that since  $CDR_p$  is obtained from copolar measurements, its estimates are available in the cloud/precipitation regions where copolar SNR values are reliable (i.e., practically everywhere where reflectivity, differential reflectivity, and copolar correlation coefficient data available) as opposed to the volumes where much weaker cross-polar SNR

are reliable as in case of “true” depolarization measurements.

As discussed above, depolarization ratios and the  $Z_{DR}$  of planar-type particles increase as radar viewing changes from vertical pointing (i.e., the  $90^\circ$  elevation angle) to slant (Fig. 1). The difference between vertical and slant values is larger for particles with a larger degree of nonsphericity (i.e., smaller  $r$  values). For the same aspect ratios, particle populations of larger size (i.e., larger  $D_{mv}$  values) exhibit smaller polarimetric variable changes compared to PSDs with smaller  $D_{mv}$  values (e.g., Fig. 1, left vs right column). This is because particle density decreases with increasing particle size, making larger particles optically “softer.” For a given aspect ratio and  $D_{mv}$  values, the influence of the  $m$ – $D$  relation choice is not very strong (e.g., Fig. 1a vs Figs. 1c,e, or Fig. 1b vs Figs. 1d,f). For a given particle characteristic size, a decrease in aspect ratios results in stronger changes to all polarimetric variables, as the direction of viewing changes from vertical to slant.

As seen in Fig. 1,  $CDR_p$  (green) and true CDR (red) values are very close to each other (as well as SLDR, which is not shown), indicating general robustness of (1). There is relatively little sensitivity of  $CDR_p$  and CDR to particle orientation parameters (i.e.,  $\sigma_\theta$ ), especially at radar elevation angles between about  $40^\circ$  and  $60^\circ$ . In contrast, LDR is very strongly dependent on particle orientation and is much lower than CDR and  $CDR_p$ . For  $\sigma_\theta = 3^\circ$ , LDR changes very little with elevation angle and is close to  $LDR_{min}$ . Term  $Z_{DR}$  also exhibits some variability depending on particle orientation but to a much smaller extent than LDR.

Modeling results from Fig. 1 correspond to moderately nonspherical particles such as aggregates and irregular ice hydrometeors. Pristine planar-type crystals (e.g., dendrites, plates) usually have aspect ratios less than about 0.1 (e.g., Pruppacher and Klett 1978) and their CDR values at slant viewing can reach maximum values of about  $-8$  dB (e.g., Reinking et al. 2002; Matrosov et al. 2001, 2012), making these habits readily identifiable by polarimetric radar measurements.

While planar-type particles typically have depolarization ratios near the  $DR_{min}$  when viewed in the vertical (or nadir) direction, columnar-type particles exhibit stronger depolarization in this direction. Experimental observations of columns and needles presented in the literature indicate depolarization values of approximately  $-15$  to  $-17$  dB (e.g., Matrosov et al. 2001, 2012; Reinking et al. 2002). Although observing columnar-type crystals is not uncommon, most scanning polarimetric radar measurements typically indicate planar-type (i.e., oblate) particle habits (e.g., Reinking et al. 2002; Marchand et al. 2013). This includes the

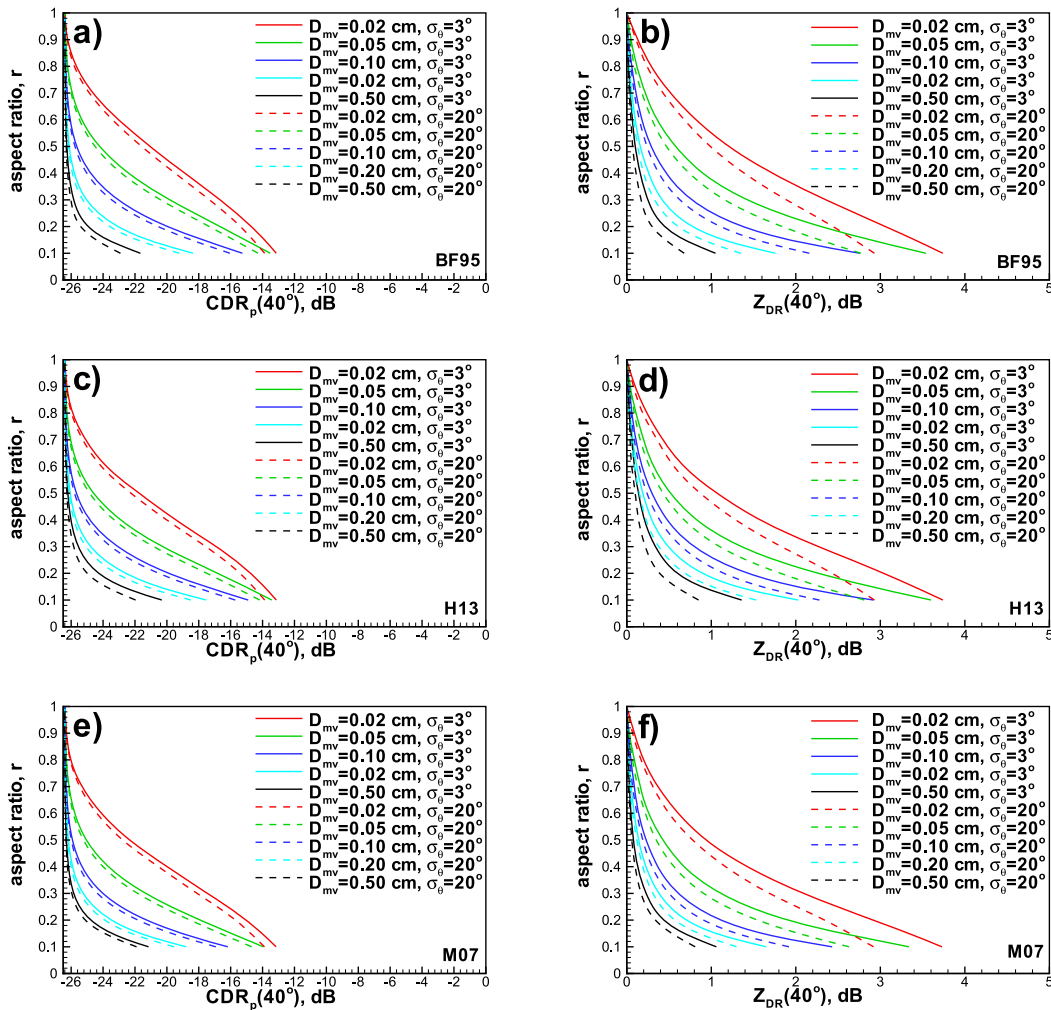


FIG. 3. Correspondence between planar-type particle aspect ratios and  $CDR_p$  and  $Z_{DR}$  at  $40^\circ$  elevation angle for different particle orientation  $\sigma_\theta$  and  $D_{mv}$  as in Fig. 1: (a),(b) BF95, (c),(d) H13, and (e),(f) M07  $m$ - $D$  relations.

populations of irregular and aggregate particles observed most frequently, as in the event considered in this study.

### 3. Approaches to estimate particle aspect ratios from polarimetric variables

As seen from Fig. 1, nonspherical particle  $CDR_p$  values are least sensitive to particle orientation at radar elevations angles  $\chi$  in an approximate interval between about  $40^\circ$  and  $60^\circ$ . Because  $CDR_p$  increases as viewing direction shifts off zenith (i.e., off  $\chi = 90^\circ$ ), more slant beam pointing directions are advantageous, as they provide larger  $CDR_p$  gradients for particles with different aspect ratios. Given the trade-offs between the desire for lower sensitivities to particle orientation and achieving stronger  $CDR_p$  signals, measurements at a

radar elevation angle of  $40^\circ$  can be considered suitable for estimating particle aspect ratios. This choice of elevation angle is also dictated by the fact that often scanning radars lack sensitivity for reliably detecting echoes at higher-altitude cloud layers at lower elevation angles (e.g., Reinking et al. 2002).

For various  $m$ - $D$  relation assumptions and the first-order gamma-function PSD, the left column of Fig. 3 shows relations between oblate-type particle aspect ratios and  $CDR_p(40^\circ)$  for different assumptions of particle characteristic sizes and orientations. Depicted data indicate the relatively small influence of particle orientation on the corresponding relations and low sensitivity to particle mass-size relation. However, the influence of  $D_{mv}$ , which can be considered a proxy for the density influence, is substantial. Presented data correspond to the Ka-band SACR frequency channel and its  $DR_{min}$ . It

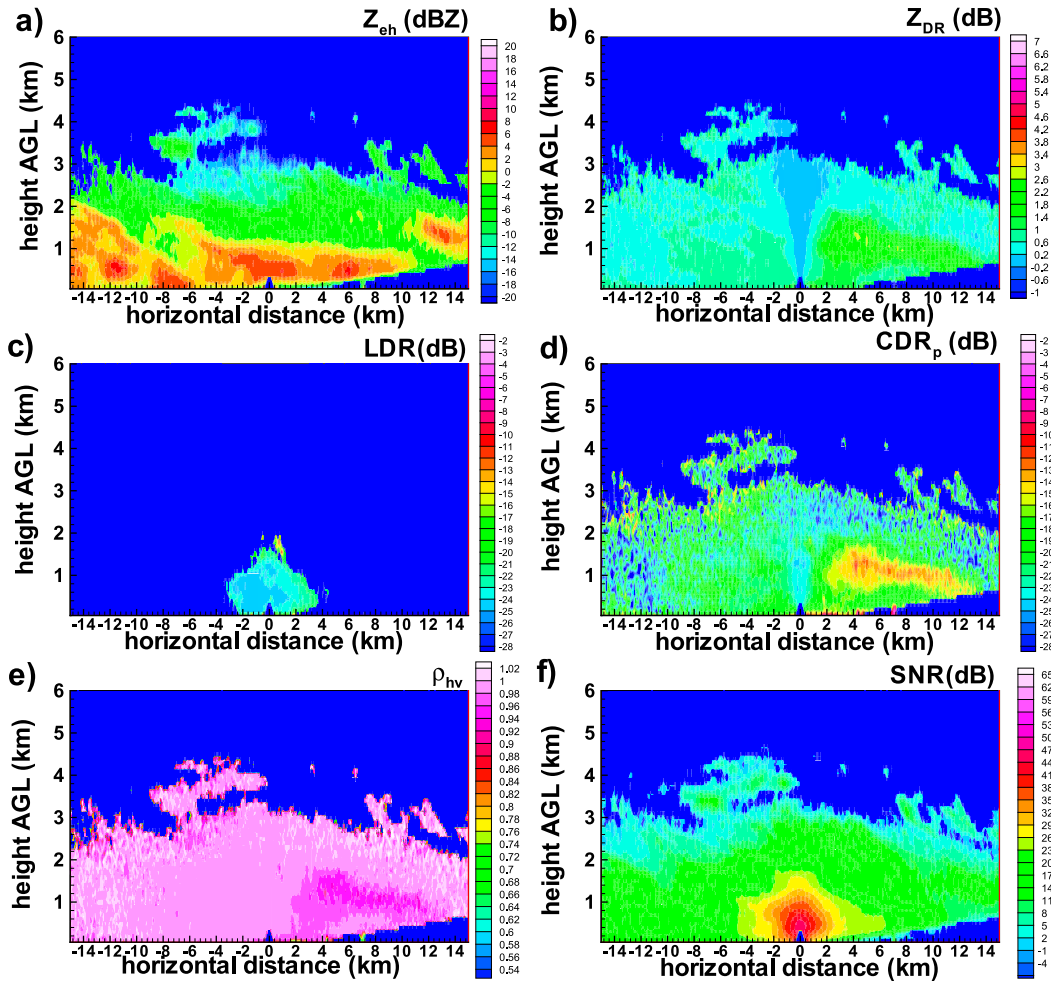


FIG. 4. Ka-band SACR RHI scans at the 135° azimuth at 0022 UTC 21 Oct 2016: (a)  $Z_{eh}$ , (b)  $Z_{DR}$ , (c) LDR, (d)  $CDR_p$ , (e)  $\rho_{hv}$ , and (f) SNR of the copolar horizontal polarization echoes.

should be noted that since  $CDR_p$  is a function of  $Z_{dr}$  and  $\rho_{hv}$ , these two variables considered together can also be used for aspect ratio retrievals. However, it is more convenient to use a single variable (i.e.,  $CDR_p$ ), which effectively combines information contained in  $Z_{dr}$  and  $\rho_{hv}$  for particle aspect ratio retrieval, and is relatively insensitive to  $\sigma_\theta$ , particularly at the elevation angle interval (40°–60°) discussed above.

As can be seen from Fig. 1, changes in  $Z_{DR}$  resulting from the variability in particle orientation generally increase as the direction of radar viewing becomes more slanted. At a 40° radar elevation angle, the variability of  $Z_{DR}$  as result of  $\sigma_\theta$  is about 2 times smaller (in logarithmic units of decibels) than at beam elevations close to 0° (i.e., almost horizontally pointing). The right column of Fig. 3 shows correspondence between  $r$  and  $Z_{DR}$  values at  $\chi = 40^\circ$ . Comparing Figs. 3a,c,e with Figs. 3b,d,f also reveals an approximately 13-dB expected range of

changes in  $CDR_p$  compared to approximately 4-dB  $Z_{DR}$  changes as values of  $r$  vary from 0.1 to 1.0. Overall, compared to  $CDR_p$ ,  $Z_{DR}$  is noticeably more sensitive to  $\sigma_\theta$  variability. When knowing or assuming  $D_{mv}$ , the modeling data from Fig. 3 can be used for estimating  $r$  of ice particles from the Ka-band SACR measurements.

#### 4. Estimating particle shapes from SACR polarimetric measurements

To test the performance of the technique discussed above, the SACR estimates of particle aspect ratios were evaluated during a period when in situ estimates of particle shapes are available from two separate systems. During October 2016, several tethered balloon system (TBS) flights were conducted at the Oliktok Point AMF3. During some of these flights, the balloon payload included the National Center for Atmospheric

Research (NCAR) VIPS (Schmitt et al. 2013). The VIPS provides information on particle size distributions and aspect ratios. In addition to the VIPS, particle in situ information was available from the ground-based MASC at Oliktok Point (Garrett et al. 2012).

The AMF3 SACR operates in 30-min cycles. Each cycle includes four hemispheric range–height indicator (RHI) scans. These scans are performed in the azimuthal directions of  $0^\circ$ ,  $45^\circ$ ,  $90^\circ$ , and  $135^\circ$  (Hardin et al. 2011). As an example, Fig. 4 shows a  $135^\circ$  SACR RHI scan conducted on 21 October 2016 during a TBS flight time (0022 UTC). The radar range gate spacing is 30 m and the first gate is 0.38 km from the radar. While the horizontal polarization radar reflectivity factor (reflectivity),  $Z_{eh}$ ,  $Z_{DR}$ , LDR, and  $\rho_{hv}$  are measured directly,  $CDR_p$  was obtained from measurable variables using (1). Because LDR values are generally very small ( $< -20$  dB) even when they can be measured, they were neglected when calculating  $CDR_p$  from observational data. The use of the  $LDR_{min}$  value in (1) results in  $CDR_p$  changes that are typically within measurement uncertainties. Since azimuthally averaged zenith-pointing differential reflectivity values are expected to be near 0 dB, a  $Z_{DR}$  measurement bias was estimated during near-vertical beam measurements ( $\chi = 90^\circ \pm 1^\circ$ ) at different RHI directions and then accounted for. For the SACR Ka-band channel, this bias was typically around 0.1 dB during the observational period considered here.

The  $Z_{eh}$ ,  $Z_{DR}$ , and  $\rho_{hv}$  data were thresholded at the 3-dB SNR level of the copolar echoes, and LDR data were thresholded at the same level in the cross-polar radar echoes. These echoes are much weaker than the copolar ones, thus LDR data are available only in the regions close to the radar (Fig. 4c).  $CDR_p$ , however, is available in the same regions where copolar echoes are reliable. Polarimetric variables are also useful in identifying ground clutter returns from infrastructure around the Oliktok facility (e.g., a small arc at about 2-km distance from the radar site in LDR measurements).

Elevated  $CDR_p$  values (approximately  $-12$  dB) in a slanted layer at an altitude of about 1 km in the azimuth direction of  $135^\circ$  (Fig. 4d) are characteristic of single dendrites or hexagonal plates (Matrosov et al. 2001; Reinking et al. 2002), indicating a dominance of these highly nonspherical planar crystal habits in this portion of the atmosphere. These enhanced  $CDR_p$  values also correspond to decreased  $\rho_{hv}$  values and higher  $Z_{DR}$  values, which is consistent with the dendrite/plate particle habit. Generally, smaller  $CDR_p$  and  $Z_{DR}$  values at lower and higher altitudes ( $< 0.8$  km and  $> 1.3$  km, respectively) suggest the dominance of moderately nonspherical particles. Such particles might be relatively rare in the layer of the increased  $CDR_p$  values (which

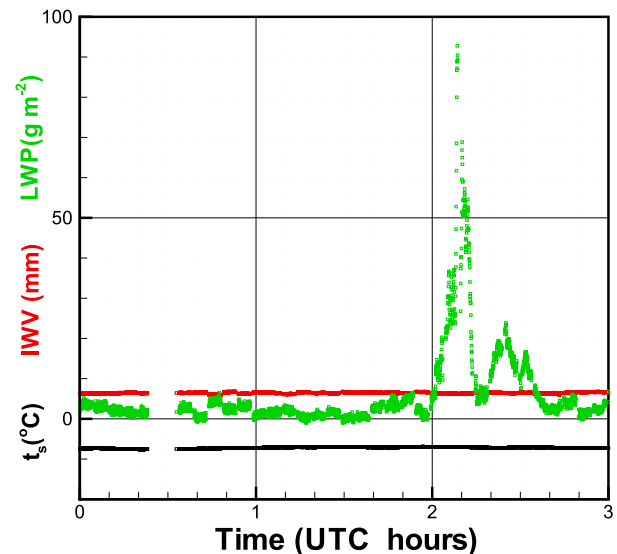


FIG. 5. Near-surface air temperature (black) and MWR-based estimates of IWV (red) and LWP (green) on 21 Oct 2016 during the TBS sounding. Data were corrected for by a “dry” bias of  $17 \text{ g m}^{-2}$ .

also corresponds to a layer of lower reflectivity), so they do not obscure the polarimetric signal of highly nonspherical planar crystals. The range of observed  $CDR_p$  values, including the layer dominated by dendrites/plates in measurements shown in Fig. 4, is about 14 dB compared to about 2.5 dB for  $Z_{DR}$ , and 3 dB for LDR.

Figure 5 shows the AMF3 microwave radiometer (MWR)-based bias-corrected estimates of liquid water path (LWP) and integrated water vapor (IWV) during the 21 October 2016 TBS flight between about 0020 and 0248 UTC (Cadeddu 2011). The LWP values are in the retrieval noise between 0000 and 0200 UTC. When coupled with the fact that no supercooled liquid cloud base was detected by lidar for these first 2 h of 21 October 2016 (not shown), this suggests that liquid water was not present during this time, so ice particle riming was not expected. This is not true for the latter portion of the TBS flight (after 0200 UTC), when modest amounts of supercooled liquid were detected by the MWR and liquid drops were present in VIPS data. Near-surface (2 m) air temperature (black line in Fig. 5) was around  $-8^\circ\text{C}$  for the duration of this sounding.

Atmospheric profiles from a radiosonde launched at the AMF3 on 2330 UTC 20 October 2016 (i.e., just prior to the TBS measurement period) are shown in Fig. 6 (Coulter et al. 1994). The data show the presence of a near-surface temperature inversion beneath the cloud-driven mixed layer and an approximately isothermal layer between 0.4 and 1 km. The winds were fairly weak throughout the hydrometeor layer. The  $-15^\circ\text{C}$  temperature, which usually associated with the pristine



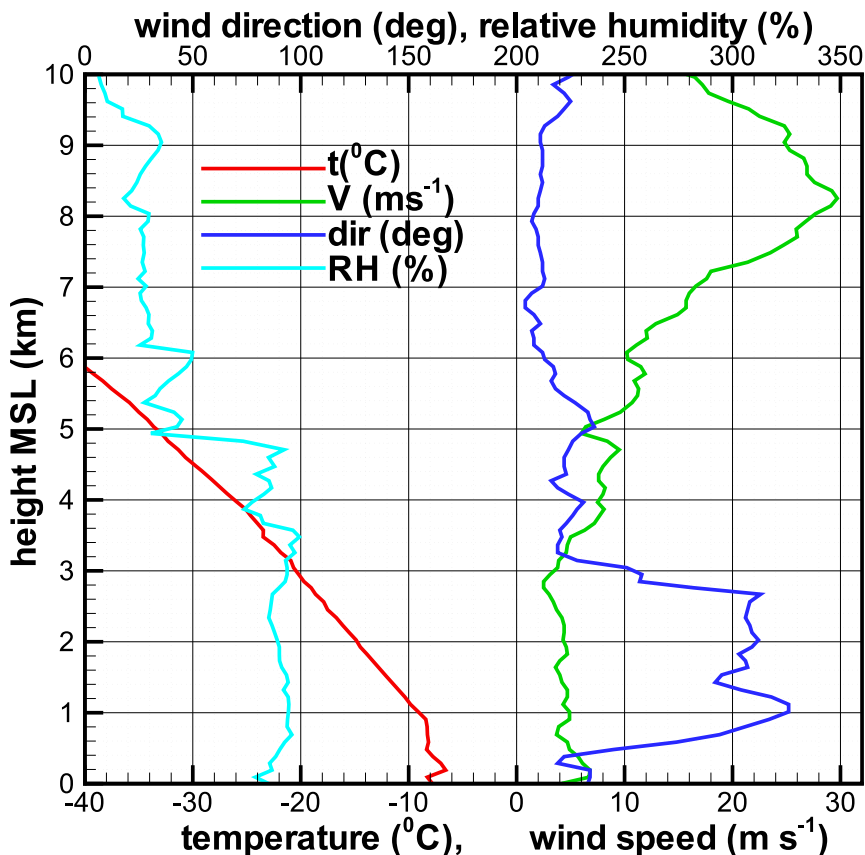


FIG. 6. Results of the radiosonde sounding at Oliktok Point at 2330 UTC 20 Oct 2016.

dendritic crystal growth is at an about 2 km altitude, which is higher than the layer of enhanced  $Z_{DR}$  and  $CDR_p$  (Fig. 4).

The TBS flight was relatively low and the maximum height available for VIPS microphysical measurements was only between 0.4 and 0.5 km. Figure 7a shows the elevation angle dependence of  $Z_{DR}$  and  $CDR_p$  at an altitude of 0.4 km, obtained during hemispheric RHI radar measurements for the scan shown in Fig. 4. The lowest  $CDR_p$  values in the vertical direction and their general increase when radar viewing shifts toward slant directions indicate a planar (oblate) particle habit. The depolarization increase is indicative of irregular and/or aggregate ice particles (e.g., Reinking et al. 2002). Although the elevation angle trends of  $Z_{DR}$  and  $CDR_p$  are often approximately symmetrical relative to the vertical pointing direction (i.e.,  $\chi = 90^\circ$ ) as in Fig. 7a, sometimes the symmetry is not observed, as shown in Fig. 7b for another RHI scan. This relative asymmetry is suggestive of horizontal changes in particle aspect ratios occurring within close proximity of the radar location. Minimal values of  $CDR_p$  are typically seen near the vertical radar pointing for all RHI azimuths, which is indicative of the

absence of the preferential alignment of particles along a specific azimuthal direction.

Values of  $Z_{DR}$  and  $CDR_p$  obtained near elevation angles of  $40^\circ$  and  $140^\circ$  (note that  $\chi = 140^\circ$  at an azimuth  $\phi$  corresponds to  $\chi = 40^\circ$  at an azimuth  $180^\circ + \phi$ ) during RHI scans were used to retrieve particle aspect ratios using the results obtained from modeling  $r$ - $CDR_p(40^\circ)$  and  $r$ - $Z_{DR}(40^\circ)$  relations shown in Fig. 3. When comparing to aspect ratios estimated from in situ measurements, the radar-based retrievals of  $r$  are further referred to as  $r_{SACR}$ .

Figure 8 shows time series of  $r_{SACR}$  retrieved from  $CDR_p$  and  $Z_{DR}$  during the period of the TBS flight on 21 October 2016, at altitudes of 0.5 and 0.3 km. For this time, there were six intervals of hemispheric RHI scanning centered at around 0020, 0047, 0115, 0143, 0210, and 0237 UTC. Each interval was about 6 min long and contains eight retrievals from two elevation angles at each of the four azimuthal directions. To reduce measurement noise,  $CDR_p$  and  $Z_{DR}$  values used for retrievals were averaged in  $2^\circ$  elevation angle intervals centered at  $\chi = 40^\circ$  and  $\chi = 140^\circ$ . The retrievals were performed under the assumption of the H13 mass-size

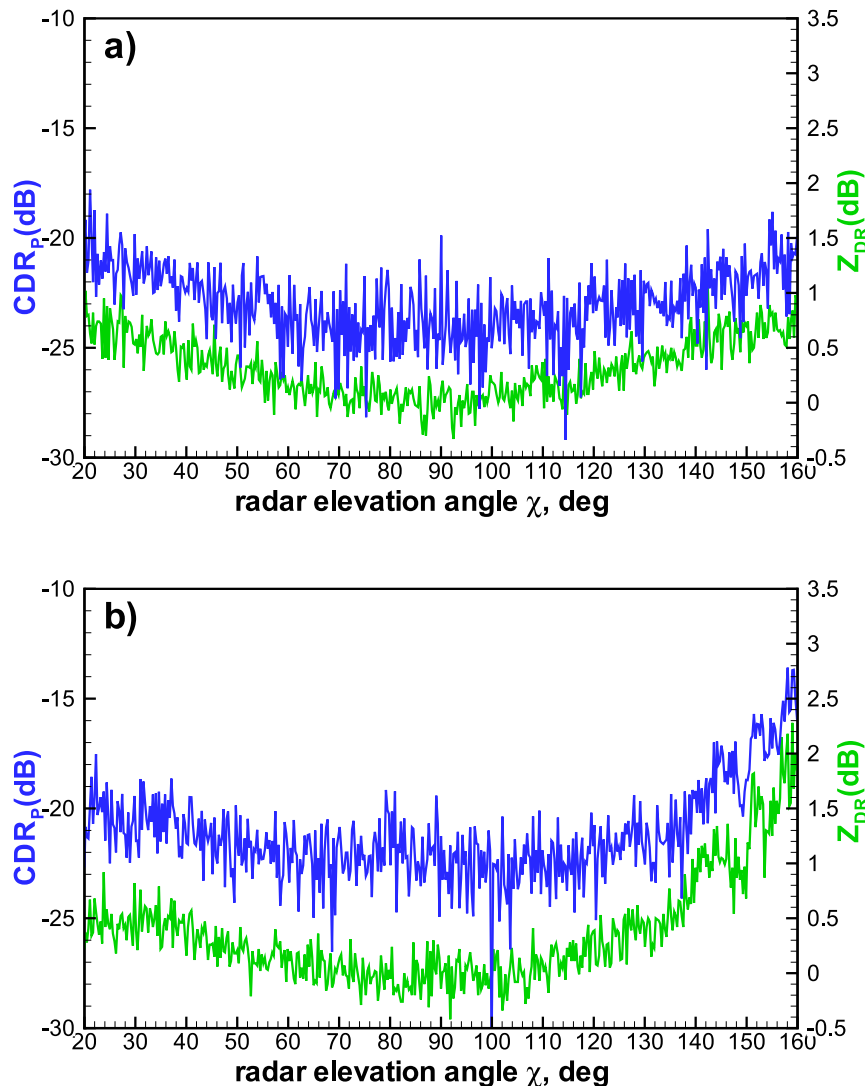


FIG. 7. Constant-altitude ( $h \approx 0.40$  km) elevation angle dependence of SACR Ka-band  $CDR_p$  and  $Z_{DR}$  at the  $135^\circ$  azimuth on 21 Oct 2016, at (a) 0022 and (b) 0212 UTC.

relation,  $\sigma_\theta = 10^\circ$ , and  $D_{mv} = 0.05$  cm. VIPS measurements indicated similar  $D_{mv}$  values, as shown in section 5.

Figure 8 indicates  $r_{SACR}$  values generally being between 0.25 and 0.55. Such aspect ratios are characteristic of aggregate/irregular ice particles, which likely dominated the radar echoes during these measurements. There is general agreement between the results from the  $CDR_p$  and  $Z_{DR}$ -based retrievals. A very weak trend of particles becoming more nonspherical with time is noticed. As seen from Fig. 8, there is not much difference between radar-based retrievals of the aspect ratio at altitudes 0.5 and 0.3 km above the radar site. Note that retrievals at very low altitudes are not possible because of the offset of the first radar range gate. When  $Z_{DR}$  and

$CDR_p$  are approximately symmetrical around the vertical direction, the values of the retrieved aspect ratios in each of the RHI sequences are relatively close to each other (e.g., 0020, 0047, 0143, and 0237 UTC). The asymmetry in  $Z_{DR}$  and  $CDR_p$  results in larger variations in aspect ratio estimates as seen for the RHI sequence conducted at about 0115 and 0210 UTC.

#### *Expected uncertainties of polarimetric radar-based aspect ratio estimates*

Uncertainties of the radar-based retrievals of particle aspect ratios come from errors in the radar variables (i.e.,  $CDR_p$  and  $Z_{DR}$ ) and from retrieval assumptions. Influential assumptions include those about PSD type,  $m$ - $D$  relations, the degree of particle orientation

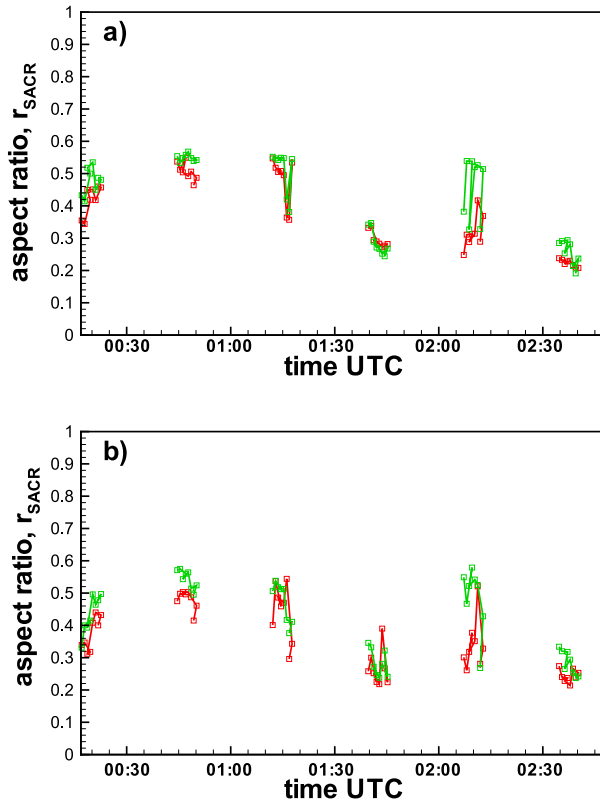


FIG. 8. Retrievals of particle aspect ratios from SACR  $CDR_p$  (red) and  $Z_{DR}$  (green) data at an altitude of (a) 0.5 and (b) 0.3 km on 21 Oct 2016. The eight data points for each observation period correspond to the eight azimuthal directions.

(e.g.,  $\sigma_\theta$ ), and characteristic PSD size (e.g.,  $D_{mv}$ ). A sensitivity analysis with the modeling approach used to calculate data in Figs. 1 and 3 was performed to assess retrieval uncertainties due to (i) variability in the assumed  $m$ - $D$  relations (among the BF95, H13, and M07 considered in Fig. 1), (ii) a  $\pm 10^\circ$  variability in the assumed  $\sigma_\theta$  value, (iii) changes in the assumed PSD type for a given  $D_{mv}$  (e.g., when the PSD gamma-function shape parameter  $\mu$  changes between 0 and 3), and (iv) a 50% uncertainty in  $D_{mv}$ . This analysis indicated that these four sources of retrieval uncertainty can result in approximately (i) 2% (10%), (ii) 7% (8%), (iii) 5% (5%), (iv) 26% (28%) errors when estimating particle aspect ratios from  $CDR_p$  ( $40^\circ$ ) [ $Z_{DR}(40^\circ)$ ] for nonsphericity values typical of aggregate hydrometeors (e.g.,  $r \approx 0.5$ ).

The data in Fig. 7 suggest that errors of around 0.5 dB (0.1 dB) in  $CDR_p$  ( $Z_{DR}$ ) values can be expected even with data averaging in the  $\pm 2^\circ$  interval.  $CDR_p$  uncertainties are similar to those of direct depolarization measurements (Fig. 2). These errors can result in about 10%–15% uncertainties in radar-based retrievals of particle aspect ratios. Assuming errors from all

uncertainty sources are independent, the resulting relative retrieval uncertainties can be estimated as a square root of the sum of squares of individual contributions. These estimates result in about 30% (35%) uncertainties for aspect ratio retrievals from  $CDR_p$  ( $40^\circ$ ) [ $Z_{DR}(40^\circ)$ ] data. For typical  $CDR_p$ -based  $r_{SACR}$  values (Fig. 8), this corresponds to expected errors of around 0.1–0.15.

As evident from the uncertainty estimates presented above and from Fig. 3, a substantial part of particle aspect ratio retrieval errors comes from uncertainties in particle characteristic size (e.g.,  $D_{mv}$ ) that can be considered as a proxy of effective density. Correspondence between  $r$  and radar polarimetric variables depends on this size, and the resulting dependences are generally a proxy for the relationships between radar variables and effective bulk density (with accounting for non-Rayleigh scattering effects) of the entire PSD (Matrosov 2015). Less dense particles produce less pronounced polarization signatures than denser particles of the same shape. Recent approaches for inferring particle aspect ratios from STSR radar measurements either assume a solid ice density or retrieve polarizability ratios, which could be converted to aspect ratios if a fixed assumption on particle density is made (e.g., Myagkov et al. 2016b; Melnikov 2017). For nonpristine ice particles, bulk density, however, generally decreases with particle size as mass–size relations suggest, so a characteristic size describing the entire particle distribution (e.g.,  $D_{mv}$ ) could be a convenient parameter reflecting bulk density (and non-Rayleigh scattering) effects on the correspondence between particle aspect ratios and radar polarimetric variables.

The Ka-band SACR-based retrievals for 21 October 2016 observations were made assuming  $D_{mv} = 0.05 \pm 0.025$  cm, which (judging from in situ VIPS measurements shown in the next section) were reasonable assumptions for this observational event. Independent particle characteristic size estimates, however, could be an essential part of future routine radar-based retrievals of particle aspect ratios. Such estimates could come from the dual-frequency reflectivity ratio (DFR) and/or dual-Doppler velocity measurements from collocated Ka-W-band SACR data when DFR signals are strong enough for larger particle populations (e.g., Matrosov 1993, 2011). Other approaches for estimating particle characteristic sizes can use relations between such sizes and observed reflectivities and/or time-averaged vertical Doppler velocities (e.g., Matrosov 1997; Matrosov et al. 2002; Matrosov and Heymsfield 2017), the higher moments of the Doppler spectrum (Maahn and Löhnert 2017), or from multisensor (e.g., radar–lidar) microphysical retrievals (e.g., Shupe et al. 2015). A detailed analysis

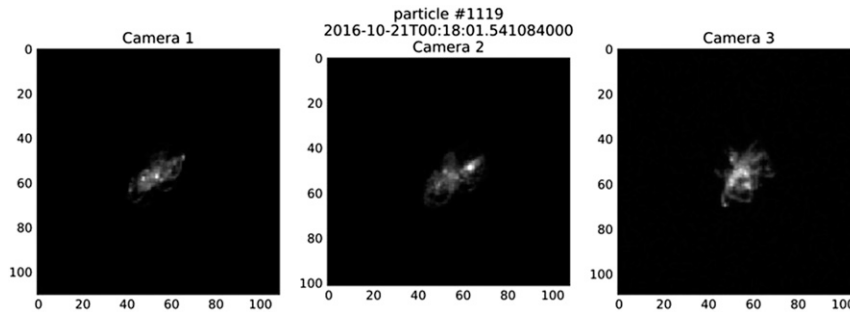


FIG. 9. An example of a particle photographed from three MASCs during the 21 Oct 2016 event.

of different approaches of particle characteristic size retrievals are outside the scope of this study.

## 5. Comparison of radar-derived particle aspect ratios with in situ estimates

### a. Comparisons with the MASC data

The MASC instrument (Garrett et al. 2012), deployed at the AMF3, captures photographs of falling particles from three different angles (Gaustad et al. 2015; dataset updated daily). The camera's resolution allows for identification of particles larger than about 0.5 mm. It provides estimates of side view particle aspect ratios, as well as particle fall velocities and the largest dimensions. As in Korolev and Isaac (2003), the aspect ratio is defined as the ratio of the maximum particle dimension from an image to the particle width, which is its dimension in the direction perpendicular to the maximum dimension. Example images of a particle with a maximum dimension of about 0.9 mm taken by the MASC during the event of 21 October 2016 are shown in Fig. 9. About 600 particles were reliably sampled by the MASC during the TBS flight on 21 October 2016. The general shape/habit of the particle in Fig. 9 is representative of irregular aggregated particles observed by the MASC during this event.

For the same time span covering the radar retrievals shown in Fig. 8, Fig. 10 shows MASC estimates of particle aspect ratios. The  $r_{\text{MASC}}$  quantity in Fig. 10 represents average MASC data:

$$r_{\text{MASC}} = \langle r_{M0} + r_{M1} + r_{M2} \rangle / 3, \quad (2)$$

where  $r_{Mi}$  ( $i = 0, 1, 2$ —is the camera identifier) are aspect ratios and angle brackets denote averaging over observed particles during a given period (5 or 10 min). Values of  $r_{\text{MASC}}$  represent the standard MASC aspect ratio product. Since the MASC provides multiple views of a given particle, additional estimates of  $r$  were

calculated. These estimates are also shown in Fig. 10. One such estimate represents a time average of the smallest aspect ratio from the three available multiangle images for a particular particle  $r_{\text{MASC1}}$ :

$$r_{\text{MASC1}} = \langle \min(r_{M0}, r_{M1}, r_{M2}) \rangle. \quad (3)$$

The mean difference between  $r_{\text{MASC}}$  and  $r_{\text{MASC1}}$  is approximately 0.1. Another  $r$  estimate from MASC images represents the minimal-to-maximal dimensions of particles as seen by all three cameras:

$$r_{\text{MASC2}} = \langle \min(D_0 r_{M0}, D_1 r_{M1}, D_2 r_{M2}) \rangle / \max(D_0, D_1, D_2), \quad (4)$$

where  $D_0$ ,  $D_1$ , and  $D_2$  are the largest particle dimensions seen by the corresponding cameras. The mean difference between  $r_{\text{MASC}}$  and  $r_{\text{MASC2}}$  is about 0.15.

Theoretical modeling of spheroidal shape 2D projections indicates that for actual  $r$  of 0.6, the mean projected  $r$  for quasi-horizontal particle orientation is about 0.75 and it is slightly higher for randomly oriented particles (Jiang et al. 2017). This agrees relatively well with the mean observed difference between  $r_{\text{MASC}}$  and  $r_{\text{MASC2}}$ .

Values of  $r_{\text{MASC1}}$  and especially  $r_{\text{MASC2}}$  obtained from MASC data could be more appropriate in situ estimates of aspect ratios for comparisons with  $r_{\text{SACR}}$  because for the given particle shape, assumption  $r_{\text{SACR}}$  represents the ratio of the smallest possible to the largest possible spheroidal model particle dimensions. The ratio of these dimensions for an idealized spheroidal particle model is generally smaller than ratios of the smallest to the largest projections of such a particle on a 2D plane (e.g., a photograph), so it can be expected that  $r_{\text{SACR}} \leq r_{\text{MASC2}} \leq r_{\text{MASC1}} \leq r_{\text{MASC}}$ . Typical  $r_{\text{MASC2}}$  estimates in Fig. 10a are between 0.4 and 0.55, while  $r_{\text{SACR}}$  values are mostly between 0.25 and 0.55 (Fig. 8). Given the radar retrieval uncertainties, the MASC estimates and the radar-derived values of particle aspect ratios are

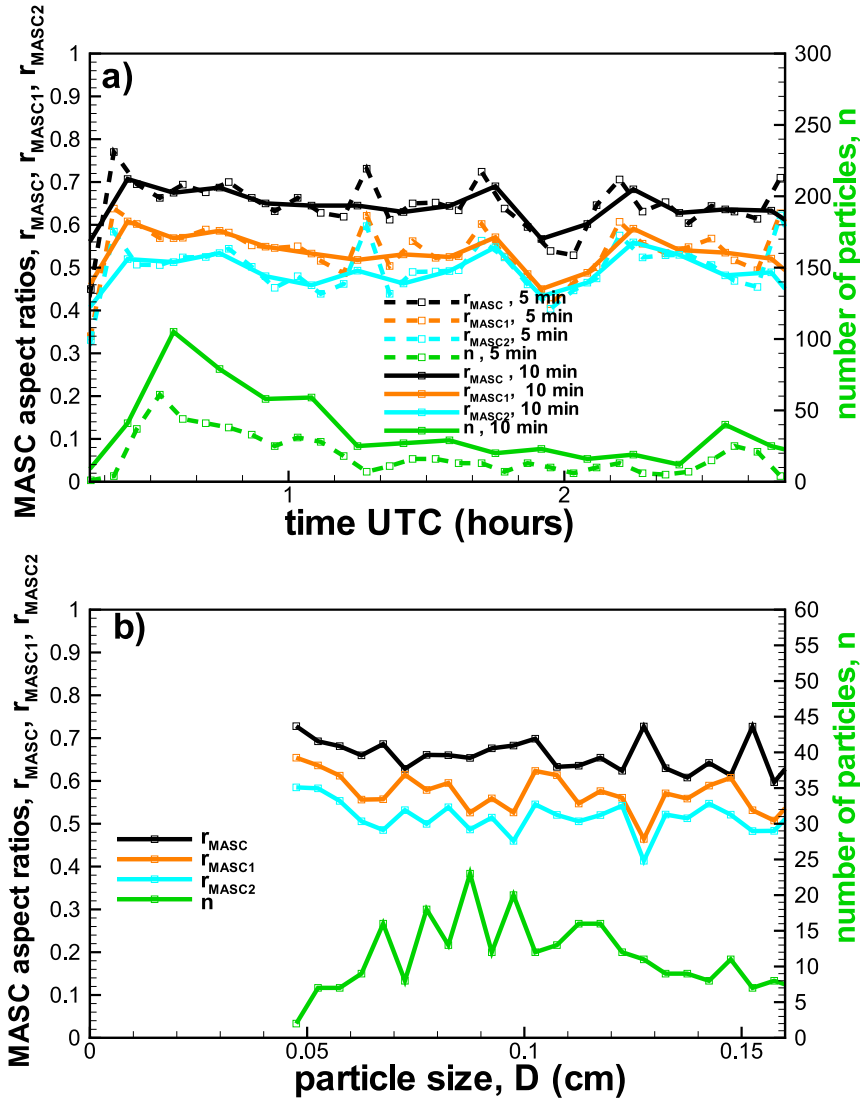


FIG. 10. (a) The 5- and 10-min averages of MASC particle aspect ratio estimates and number of observed particles, and (b) the mean MASC aspect ratios as a function of particle size and number of particles averaged for each size interval. Observations during TBS soundings on 21 Oct 2016.

consistent. The vastly different sampling volumes of radar and in situ data and the differing measurement schemes and locations make exact point-to-point comparisons impossible.

Because of the relatively small number of particles observed by the MASC and the underrepresentation of particles with sizes less than about 0.5 mm (see Fig. 10b), the data in Fig. 10a represent mean values for particles of all sizes that were reliably observed by the MASC for a given averaging period. It can be seen from Fig. 10a that the difference between the averaging windows (5 min vs 10 min) does not significantly influence the results. As also seen from Fig. 10b, the different particle

aspect ratios observed by the MASC (i.e.,  $r_{MASC}$ ,  $r_{MASC1}$ ,  $r_{MASC2}$ ) did not exhibit strong size dependence, justifying the intercomparison of MASC-observed and radar-derived reflectivity-weighted particle aspect ratios. The mean aspect ratios in Fig. 10b represent averages for the whole TBS flight period on 21 October 2016.

*b. Comparisons with the VIPS data*

The VIPS microphysical probe was mounted on the TBS. Environmental conditions restricted TBS operations, limiting the maximum altitude of VIPS operation to approximately 0.5 km. Figure 11 depicts examples of 2D images of ice particles sampled by the VIPS on

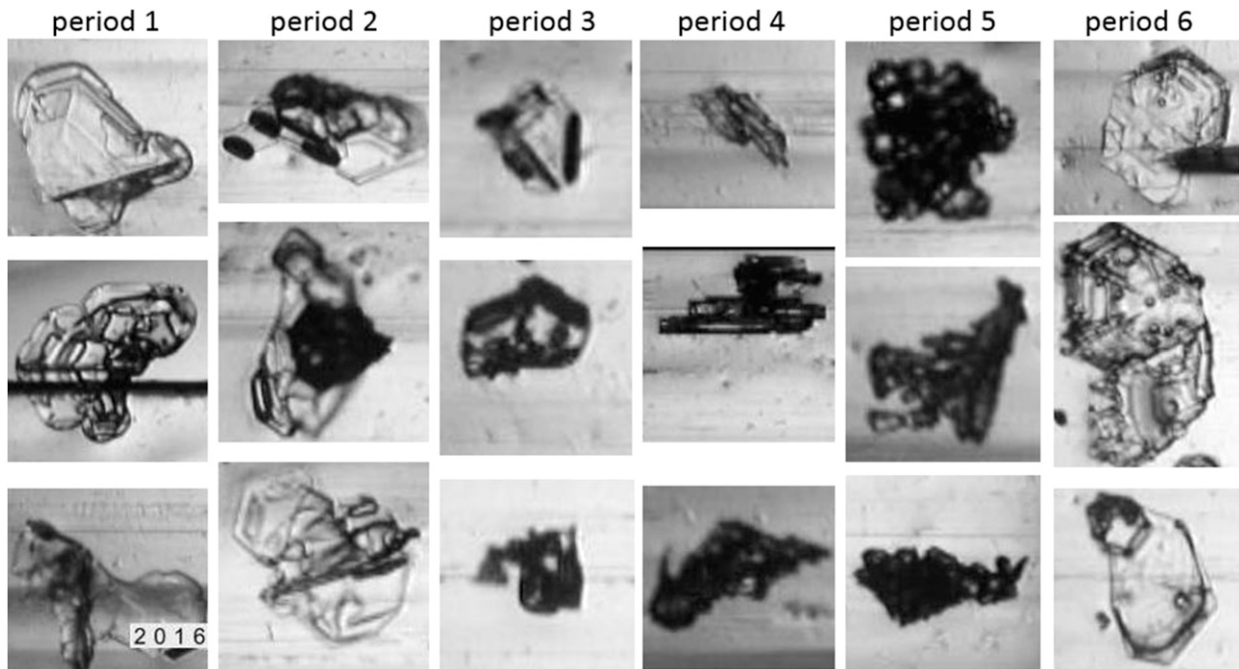


FIG. 11. Examples of ice particles sampled by the VIPs on 21 Oct 2016 for six periods of SACR RHI scans: 0017–0023, 0044–0050, 0112–0118, 0140–0146, 0207–0213, and 0234–0240 UTC, respectively.

21 October 2016 during six periods of SACR RHI scans. As was the case with the MASC measurements, particles detected by the VIPs were also generally irregular in shape, with many aggregates. With the exception of period 5 (~0207–0213 UTC), there was little evidence of riming. During period 5, which corresponds to elevated LWP values (Fig. 5), the VIPs also sampled some spherical supercooled water drops (not shown). Aggregates of hexagonal plates and some pristine crystals are seen among irregularly shaped particles, especially during period 6 (~0234–0240 UTC). This is not necessarily surprising, as there was evidence of a layer of single pristine plates/dendrites from radar measurements in Fig. 4 at altitudes above 1 km.

While the MASC measurements were not used for deriving particle size distributions as a result of the undersampling of smaller particles and the relatively small total number of observed particles, VIPs data can provide such distributions (50- $\mu\text{m}$  equally spaced bins between 0 and 2 mm). Mean PSDs derived from VIPs during the six 6-min periods of SACR RHI scan sequences on 21 October 2016 are shown in Fig. 12. It can be seen that particle major projectional dimensions did not generally exceed 0.1 cm, suggesting that non-Rayleigh scattering effects at Ka band were likely rather small. Median volume particle sizes of these distributions were around  $0.06 \pm 0.02$  cm, justifying the  $D_{mv}$  assumption made for the radar-based retrievals.

For the same time interval as in Fig. 12, Fig. 13 shows mean VIPs-derived particle aspect ratios  $r_{VIPs}$  inferred from 2D images as a function of particle size. The standard deviations of aspect ratios, which characterize in situ estimate uncertainties, were generally between 0.15 and 0.2. Further, Fig. 13 demonstrates that, as for particles observed by the MASC, mean  $r_{VIPs}$  does not exhibit a clear trend with particle size (except, probably, for the 0140–0146 UTC period). The fact that variability in  $r$  with particle size (for particles larger than about 0.1 cm) is relatively small can also be deduced from the data presented by Korolev and Isaac (2003).

Figure 14a shows mean reflectivity-weighted  $r_{VIPs}$  estimates and corresponding mean VIPs probe heights during the periods corresponding to the radar-based retrievals in Fig. 8. The width of the square symbols in Fig. 14 corresponds to the time interval of the SACR RHI scan sequence. The  $r_{VIPs}$  values vary from about 0.3 to 0.77 and are on average a little higher than  $r_{SACR}$ . The lack of multiangle particle views for the VIPs samples precludes estimates of how  $r_{VIPs}$  values would change depending on the choice of projections used [as from Eqs. (3) and (4)]. If, however, it is assumed that the corresponding changes are like those deduced from the MASC multiangle aspect ratio estimates, then a reduction of  $r_{VIPs}$  of around 0.1–0.15 would be expected. This reduction could be even larger specifically for the VIPs data during the period 6 (0234–0240 UTC) because the sampled particle habit during this

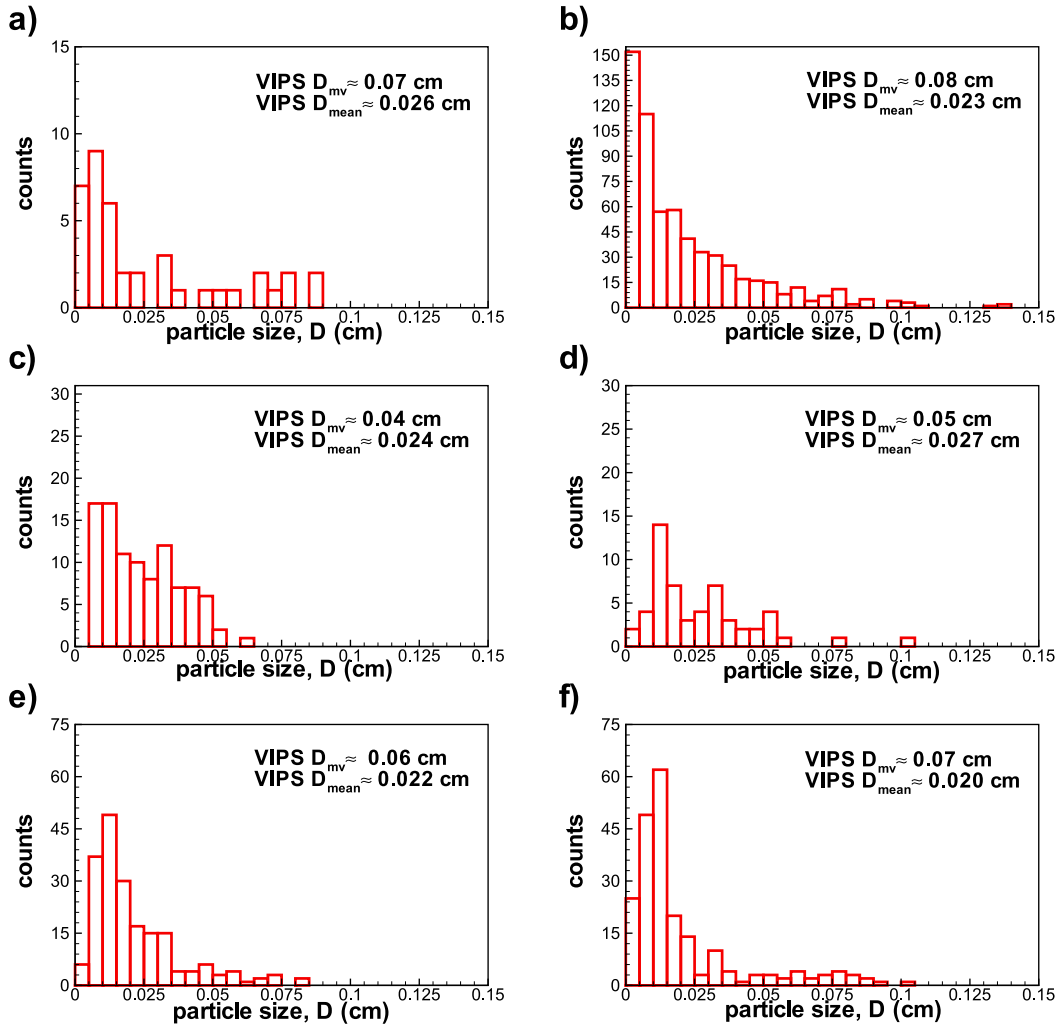


FIG. 12. Particle size distributions derived from the VIPS measurements on 21 Oct 2016 for periods (a) 0017–0023, (b) 0044–0050, (c) 0112–0118, (d) 0140–0146, (e) 0207–0213, and (f) 0234–0240 UTC.

period included a substantial number of aggregates of plates (see Fig. 11). Term  $r_{VIPS}$  in this case could be exaggerated, since the smallest dimensions of such particles are not typically seen in VIPS single-plane 2D images.

Figure 14b presents composite intercomparisons of hydrometeor aspect ratios from remote and situ observations. Radar-retrieved values correspond to 0.5-km altitude. Overall, it can be concluded that, given uncertainties of the retrievals and direct estimates (as expressed by their standard deviations) and some spatial displacement of the data, in situ aspect ratio estimates for the considered dataset are consistent with  $r_{SACR}$ . The largest discrepancies with VIPS data are seen for the first ( $\sim$ 0017–0023 UTC) and the last ( $\sim$ 0234–0240 UTC) comparison periods when VIPS measurements were conducted near the ground during the TBS ascent and descent. For these periods,  $r_{VIPS}$  were larger than those derived from radar measurements and MASC

data. This discrepancy, in part, can be explained by the presence of aggregates (and occasional pristine types) of hexagonal plates in relatively significant numbers during these periods and the way the VIPS 2D images often are not representative of the smallest dimensions of such particles. One could expect that this also would lead to an increase of differences between various estimates of aspect ratios from the MASC. However, this is not supported by the MASC observations (Fig. 10), so the reason for the increased discrepancies during these periods remains unclear.

## 6. Conclusions

This study presents a novel method to mean estimate aspect ratio ( $r$ ) of planar-type (oblate) ice hydrometeors from scanning polarimetric radar observations. The approaches suggested here for using scanning polarimetric

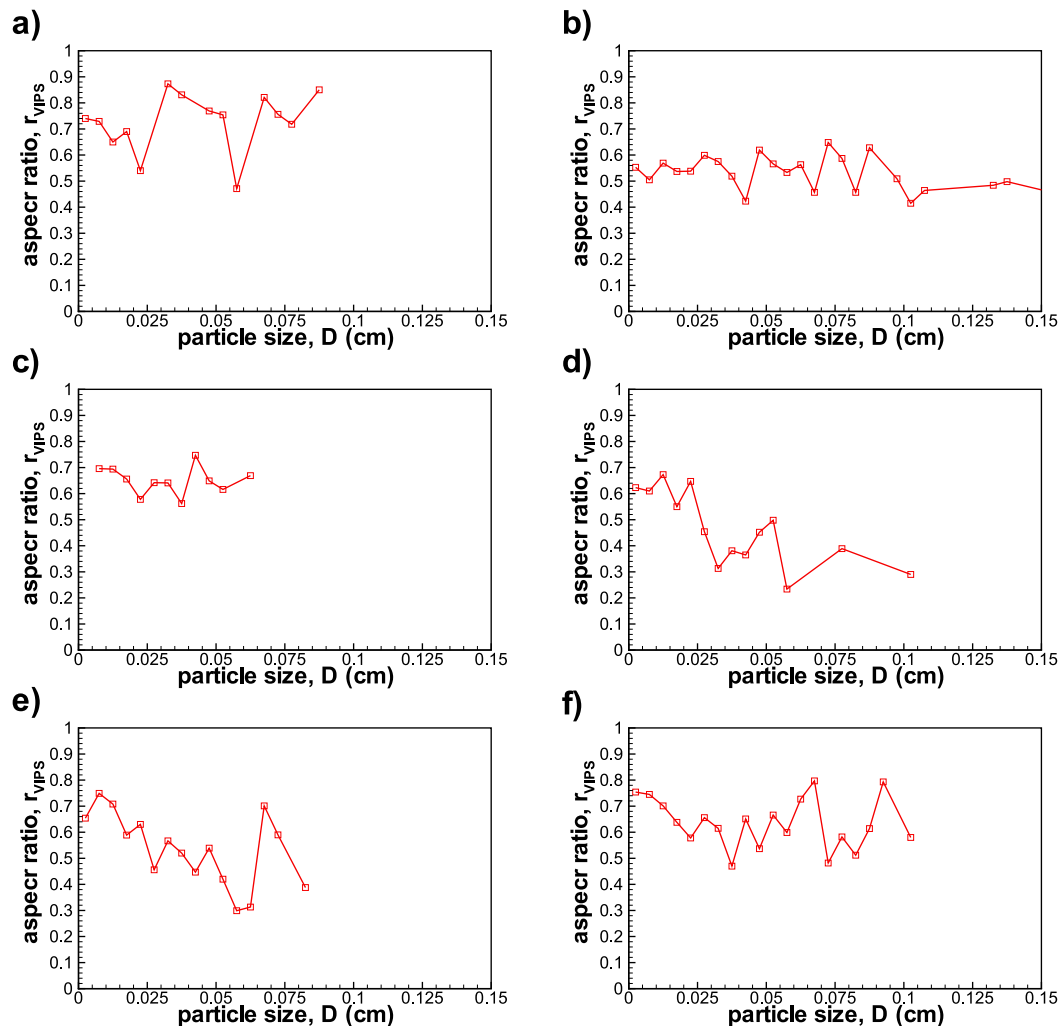


FIG. 13. VIPS particle aspect ratio estimates on 21 Oct 2016 for periods (a) 0017–0023, (b) 0044–0050, (c) 0112–0118, (d) 0140–0146, (e) 0207–0213, and (f) 0234–0240 UTC.

radar measurements to infer  $r$  utilize measurements from ARM cloud radars operating in a fully polarimetric alternate horizontal-vertical polarization transmission mode. This avoids polarization coupling that would otherwise complicate measurement interpretation. Combining differential reflectivity  $Z_{DR}$  and copolar coefficient  $\rho_{hv}$  measurements allows for reconstruction of a circular depolarization ratio proxy  $CDR_p$ . This proxy is generally insensitive to particle orientation variability (flutter) if observed at elevation angles between  $40^\circ$  and  $50^\circ$ , and is immune to propagation effects resulting from accumulation of the differential phase. Term  $CDR_p$  effectively combines information contained in  $Z_{DR}$  and  $\rho_{hv}$ , providing practical convenience in estimating particle aspect ratios. Besides the relative insensitivity to particle orientation, use of  $CDR_p$  is preferred over the measured linear depolarization ratio (LDR) because of its greater range, which is as large

as for copolar radar measurements. The planar-type hydrometeors are observed much more often than the columnar-type hydrometeors (e.g., Marchand et al. 2013). These two hydrometeor types can be distinguished from each other by the  $CDR_p$  elevation angle dependences (e.g., Matrosov et al. 2001, 2012). The method can potentially be extended for the use with CDR estimates obtained from radar measurements utilizing the simultaneous transmission-reception mode (e.g., Ryzhkov et al. 2017).

Two approaches for inferring  $r$  from the Ka-band SACR measurements were evaluated in this study: one used  $CDR_p$  values at a  $40^\circ$  elevation angle and the other used  $Z_{DR}$  measurements at the same radar elevation angle. Compared to  $CDR_p$ ,  $Z_{DR}$  measurements are inherently more sensitive to particle orientation. These approaches were evaluated using a case study from the ARM Olightok Point facility on 21 October 2016



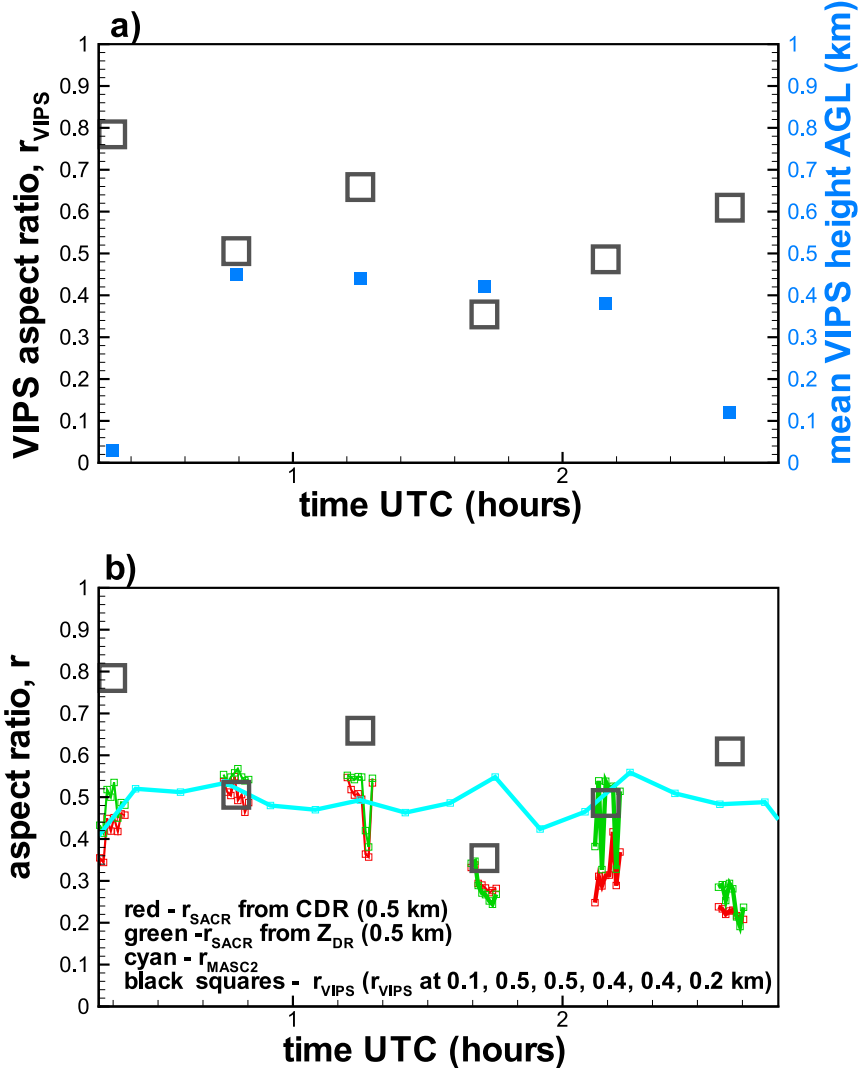


FIG. 14. (a) Mean reflectivity-weighted VIPs particle aspect ratio estimates (black squares) and corresponding sampling heights (blue squares) for the periods corresponding to SACR RHI data in Fig. 8 (i.e., 0017–0023, 0044–0050, 0112–0118, 0140–0146, 0207–0213, and 0234–0240 UTC 21 Oct 2016). (b) A composite comparison of particle aspect ratios obtained from radar and in situ measurements.

featuring TBS operations. Elevation angle patterns of depolarization indicated a dominance of planar-type (oblate) crystals during this period. While radar observations suggested the existence of layers consisting of pristine planar crystals at altitudes higher than about 1 km, lower regions, where TBS-based VIPs and surface-based MASC measurements were available, generally contained irregular/aggregated particles. Radar-based retrievals indicated characteristic aspect ratios between about 0.25 and 0.55 in this region. The  $CDR_p$ - and  $Z_{DR}$ -based retrievals were generally consistent, though estimated uncertainties for  $CDR_p$  retrievals are expected to be smaller as a result of lesser sensitivity of  $CDR_p$  to particle orientation.

MASC- and VIPs-based measurements revealed that average ice particle aspect ratios were generally between about 0.3 and 0.77. An analysis of the MASC aspect ratio variability with respect to the viewing angle and the minimum/maximum dimension choice (i.e.,  $r_{MASC1}$ ,  $r_{MASC2}$ ) indicates that actual aspect ratios of irregular/aggregated particles defined in terms of the smallest and the largest observed dimensions are smaller, in a mean sense, than the average values representing the standard MASC product (i.e.,  $r_{MASC}$ ) by about 0.1–0.15. This approximately agrees with theoretical modeling results. Standard deviations of in situ aspect ratio estimates are around 0.15–0.2.

Radar-based retrievals of particle aspect ratios ( $r_{\text{SACR}}$ ) for the TBS sounding period generally varied between about 0.25 and 0.55. Given retrieval uncertainties of about 0.1–0.15, the radar-based values are consistent with in situ observations, especially if mean in situ data are adjusted (by about 0.15) for the fact that the average observed in situ  $r$  are larger than actual minimal-to-maximal dimension ratios. Since the spheroidal  $r$  values represent the smallest possible 2D projectional aspect ratios retrieved from radar measurements,  $r$  values could be even smaller than adjusted average aspect ratio values from in situ observations. Overall, it can be concluded that polarimetric radar-based retrievals can provide particle aspect ratio information that is comparable to that obtained from in situ sampling.

**Acknowledgments.** This study was sponsored by the U.S. Department of Energy Atmospheric System Research Program under Award DE-SC0013306. We would like to acknowledge the work of the ARM-supported AMF3 operators and operations team, ARM radar technicians, and the ARM TBS operators and field scientists (Darielle Dexheimer, Albert Bendure, Jasper Hardesty, Erich Havner, Matthew Shupe) for providing the measurements used in this study. Funding for VIPS measurements and analysis was provided by the DOE ARM/ASR through Subcontract 298377 with Pacific Northwest National Laboratory of the Battelle Memorial Institute. The SACR, MASC, radiosonde, and VIPS data are available from the ARM archive.

## REFERENCES

- Avramov, A., and J. Y. Harrington, 2010: Influence of parameterized ice habit on simulated mixed phase Arctic clouds. *J. Geophys. Res.*, **115**, D03205, doi:10.1029/2009JD012108.
- Brown, P. R. A., and P. N. Francis, 1995: Improved measurements of the ice water content in cirrus using a total-water probe. *J. Atmos. Oceanic Technol.*, **12**, 410–414, doi:10.1175/1520-0426(1995)012<0410:IMOTIW>2.0.CO;2.
- Cadeddu, M., 2011: ARM: Microwave radiometer, 3 channel (OLIMWR3C). Atmospheric Radiation Measurement Climate Research Facility Data Archive. Subset used: 70°29'42.89"N, 149°53'12.78"W: Oliktok Point Mobile Facility (M1), accessed 21 October 2016, doi:10.5439/1025248.
- Coulter, R., J. Kyrouac, and D. Holdridge, 1994: ARM: Balloon-borne sounding system (BBSS): Vaisala-processed winds, pressure, temperature, and RH (SONDEWNP). Atmospheric Radiation Measurement Climate Research Facility Data Archive. Subset used: 70°29'42.89"N, 149°53'12.78"W: Oliktok Point Mobile Facility (M1), accessed 20 October 2016, doi:10.5439/1021460.
- Doviak, R. J., V. Bringi, A. Ryzhkov, A. Zahrai, and D. Zrnić, 2000: Considerations for polarimetric upgrades to operational WSR-88D radars. *J. Atmos. Oceanic Technol.*, **17**, 257–278, [https://doi.org/10.1175/1520-0426\(2000\)017<0257:CFPUTO>2.0.CO;2](https://doi.org/10.1175/1520-0426(2000)017<0257:CFPUTO>2.0.CO;2).
- Garrett, T. J., C. Fallgatter, K. Shkurko, and D. Howlett, 2012: Fall speed measurement and high-resolution multi-angle photography of hydrometeors in free fall. *Atmos. Meas. Tech.*, **5**, 2625–2633, doi:10.5194/amt-5-2625-2012.
- , S. E. Yuter, C. Fallgatter, K. Shkurko, S. R. Rhodes, and J. L. Endies, 2015: Orientations and aspect ratios of falling snow. *Geophys. Res. Lett.*, **42**, 4617–4622, doi:10.1002/2015GL064040.
- Gaustad, K., K. Shkurko, and T. Garrett, 2015: ARM: Multi-angle snowflake camera, analysis per particle (images and their aggregation) (MASCARTICLES). Atmospheric Radiation Measurement Climate Research Facility Data Archive. Subset used: 70°29'42.89"N, 149°53'12.78"W: Oliktok Point Mobile Facility (M1), accessed 21 October 2016, doi:10.5439/1350635.
- Hardin, J., D. Nelson, I. Lindenmaier, B. Isom, K. Johnson, A. Matthews, and N. Bharadwaj, 2011: ARM: Ka-band scanning ARM cloud radar hemispherical sky RHI scan (KASACRHSRH). Atmospheric Radiation Measurement Climate Research Facility Data Archive. Subset used: 70°N29'42.89"N, 149°53'12.78"W: Oliktok Point Mobile Facility (M1), accessed 21 October 2016, doi:10.5439/1046197.
- Heymsfield, A. J., C. Schmitt, and A. Bansemmer, 2013: Ice cloud particle size distributions and pressure-dependent terminal velocities from in situ observations at temperatures from 0° to –86°C. *J. Atmos. Sci.*, **70**, 4123–4154, doi:10.1175/JAS-D-12-0124.1.
- , S. Y. Matrosov, and N. B. Wood, 2016: Toward improving ice water content and snow rate retrievals from radars. Part I: X and W bands, emphasizing *CloudSat*. *J. Appl. Meteor. Climatol.*, **55**, 2063–2090, doi:10.1175/JAMC-D-15-0290.1.
- Hogan, R. J., and C. D. Westbrook, 2014: Equation for the microwave backscatter cross section of aggregate snowflakes using the self-similar Rayleigh–Gans approximation. *J. Atmos. Sci.*, **71**, 3292–3301, doi:10.1175/JAS-D-13-0347.1.
- , L. Tian, P. R. A. Brown, C. D. Westbrook, A. J. Heymsfield, and J. D. Eastment, 2012: Radar scattering from ice aggregates using the horizontally aligned oblate spheroid approximation. *J. Appl. Meteor. Climatol.*, **51**, 655–671, doi:10.1175/JAMC-D-11-074.1.
- Jameson, A. R., 1987: Relations among linear and circular polarization parameters measured in canted hydrometeors. *J. Atmos. Oceanic Technol.*, **4**, 634–645, doi:10.1175/1520-0426(1987)004<0634:RALACP>2.0.CO;2.
- Jensen, A. A., J. Y. Harrington, H. Morrison, and J. A. Milbrandt, 2017: Predicting ice shape evolution in a bulk microphysics model. *J. Atmos. Sci.*, **74**, 2081–2104, doi:10.1175/JAS-D-16-0350.1.
- Jiang, Z., M. Oue, J. Verlinde, E. Clothiaux, K. Aydin, G. Botta, and Y. Lu, 2017: What can we conclude about real aspect ratios of ice particle aggregates from two-dimensional images? *J. Appl. Meteor. Climatol.*, **56**, 725–734, doi:10.1175/JAMC-D-16-0248.1.
- Kokhanovsky, A., and A. Macke, 1999: The dependence of the radiative characteristics of optically thick media on the shape of particles. *J. Quant. Spectrosc. Radiat. Transfer*, **63**, 393–407, doi:10.1016/S0022-4073(99)00027-8.
- Kollias, P., N. Bharadwaj, K. Widener, I. Jo, and K. Johnson, 2014: Scanning ARM cloud radars: Operational sampling strategies. *J. Atmos. Oceanic Technol.*, **31**, 569–582, doi:10.1175/JTECH-D-13-00044.1.
- Korolev, A. V., and G. A. Isaac, 2003: Roundness and aspect ratio of particles in ice clouds. *J. Atmos. Sci.*, **60**, 1795–1808, doi:10.1175/1520-0469(2003)060<1795:RAAROP>2.0.CO;2.
- , ———, and J. Hallett, 1999: Ice particle habits in Arctic clouds. *Geophys. Res. Lett.*, **26**, 1299–1302, doi:10.1029/1999GL000232.

- Kosarev, A. L., and I. P. Mazin, 1991: An empirical model of the physical structure of upper-layer clouds. *Atmos. Res.*, **26**, 213–228, doi:10.1016/0169-8095(91)90055-2.
- Kropfli, R. A., B. W. Bartram, and S. Y. Matrosov, 1990: The upgraded WPL dual-polarization 8-mm Doppler radar for microphysical and climate research. Preprints, *Conf. on Cloud Physics*, San Francisco, CA, Amer. Meteor. Soc., 341–345.
- Leinonen, J., S. Kneifel, D. Moisseev, J. Tyynela, S. Tanelli, and T. Nousiainen, 2012: Evidence of nonspheroidal behavior in millimeter-wavelength radar observations of snowfall. *J. Geophys. Res.*, **117**, D18205, doi:10.1029/2012JD017680.
- Maahn, M., and U. Löhnert, 2017: Potential of higher-order moments and slopes of the radar Doppler spectrum for retrieving microphysical and kinematic properties of Arctic ice clouds. *J. Appl. Meteor. Climatol.*, **56**, 263–282, doi:10.1175/JAMC-D-16-0020.1.
- Magono, C., and T. Nakamura, 1965: Aerodynamic studies of falling snowflakes. *J. Meteor. Soc. Japan*, **43**, 139–147, doi:10.2151/jmsj1965.43.3\_139.
- Marchand, R., G. G. Mace, A. G. Hallar, I. B. McCubbin, S. Y. Matrosov, and M. D. Shupe, 2013: Enhanced radar backscattering due to oriented ice particles at 95 GHz during Storm-VEx. *J. Atmos. Oceanic Technol.*, **30**, 2336–2351, doi:10.1175/JTECH-D-13-00005.1.
- Matrosov, S. Y., 1993: Possibilities of cirrus particle sizing from dual-frequency radar measurements. *J. Geophys. Res.*, **98**, 20 675–20 683, doi:10.1029/93JD02335.
- , 1997: Variability of microphysical parameters in high-altitude ice clouds: Results of the remote sensing method. *J. Appl. Meteor.*, **36**, 633–648, doi:10.1175/1520-0450-36.6.633.
- , 2007: Modeling backscatter properties of snowfall at millimeter wavelengths. *J. Atmos. Sci.*, **64**, 1727–1736, doi:10.1175/JAS3904.1.
- , 2011: Feasibility of using radar differential Doppler velocity and dual-frequency ratio for sizing particles in thick ice clouds. *J. Geophys. Res.*, **116**, D17202, doi:10.1029/2011JD015857.
- , 2015: Evaluations of the spheroidal particle model for describing cloud radar depolarization ratios of ice hydrometeors. *J. Atmos. Oceanic Technol.*, **32**, 865–879, doi:10.1175/JTECH-D-14-00115.1.
- , and A. J. Heymsfield, 2017: Empirical relations between size parameters of ice hydrometeor populations and radar reflectivity. *J. Appl. Meteor. Climatol.*, **56**, 2479–2488, doi:10.1175/JAMC-D-17-0076.1.
- , R. F. Reinking, R. A. Kropfli, B. E. Martner, and B. W. Bartram, 2001: On the use of radar depolarization ratios for estimating shapes of ice hydrometeors in winter clouds. *J. Appl. Meteor.*, **40**, 479–490, doi:10.1175/1520-0450(2001)040<0479:OTUORD>2.0.CO;2.
- , A. V. Korolev, and A. J. Heymsfield, 2002: Profiling cloud ice mass and particle characteristic size from Doppler radar measurements. *J. Atmos. Oceanic Technol.*, **19**, 1003–1018, doi:10.1175/1520-0426(2002)019<1003:PCIMAP>2.0.CO;2.
- , R. F. Reinking, and I. V. Djalalova, 2005: Inferring fall attitudes of pristine dendritic crystals from polarimetric radar data. *J. Atmos. Sci.*, **62**, 241–250, doi:10.1175/JAS-3356.1.
- , G. G. Mace, R. Marchand, M. D. Shupe, A. G. Hallar, and I. B. McCubbin, 2012: Observations of Ice crystal habits with a scanning polarimetric W-band radar at slant linear depolarization ratio mode. *J. Atmos. Oceanic Technol.*, **29**, 989–1008, doi:10.1175/JTECH-D-11-00131.1.
- Melnikov, V., 2017: Parameters of ice cloud particles retrieved from radar data. *J. Atmos. Oceanic Technol.*, **34**, 717–728, doi:10.1175/JTECH-D-16-0123.1.
- , and S. Y. Matrosov, 2013: Estimations of aspect ratios of ice cloud particles with the WSR-88D radar. *36th Conf. on Radar Meteorology*, Breckenridge, CO, Amer. Meteor. Soc., 245, <https://ams.confex.com/ams/36Radar/webprogram/Paper228291.html>.
- , and J. M. Straka, 2013: Axis ratios and flutter angles of cloud ice particles: Retrievals from radar data. *J. Atmos. Oceanic Technol.*, **30**, 1691–1703, doi:10.1175/JTECH-D-12-00212.1.
- Mishchenko, M. I., and L. D. Travis, 1994: T-matrix computations of light scattering by large spheroidal particles. *Opt. Commun.*, **109**, 16–21, doi:10.1016/0030-4018(94)90731-5.
- Myagkov, A., P. Seifert, M. Bauer-Pfundstein, and U. Wandinger, 2016a: Cloud radar with hybrid mode towards estimation of shape and orientation of ice crystals. *Atmos. Meas. Tech.*, **9**, 469–489, doi:10.5194/amt-9-469-2016.
- , —, U. Wandinger, J. Buehl, and R. Engelmann, 2016b: Relationship between temperature and apparent shape of pristine ice crystals derived from polarimetric cloud radar observations during the ACCEPT campaign. *Atmos. Meas. Tech.*, **9**, 3739–3754, doi:10.5194/amt-9-3739-2016.
- Pruppacher, H. R., and J. D. Klett, 1978: *Microphysics of Clouds and Precipitation*. D. Reidel, 714 pp., doi:10.1007/978-94-009-9905-3.
- Reinking, R. F., S. Y. Matrosov, R. A. Kropfli, and B. W. Bartram, 2002: Evaluation of a 45° slant quasi-linear radar polarization for distinguishing drizzle droplets, pristine ice crystals, and less regular ice particles. *J. Atmos. Oceanic Technol.*, **19**, 296–321, doi:10.1175/1520-0426-19.3.296.
- Ryzhkov, A., and Coauthors, 2017: Estimation of depolarization ratio using weather radars with simultaneous transmission / reception. *J. Appl. Meteor. Climatol.*, **56**, 1797–1816, doi:10.1175/JAMC-D-16-0098.1.
- Schmitt, C. G., M. Stuefer, A. J. Heymsfield, and C. K. Kim, 2013: The microphysical properties of ice fog measured in urban environments of Interior Alaska. *J. Geophys. Res. Atmos.*, **118**, 11 136–11 147, doi:10.1002/jgrd.50822.
- Sheridan, L. M., J. Y. Harrington, D. Lamb, and K. Sulia, 2009: Influence of ice crystal aspect ratio on the evolution of ice size spectra during vapor deposition growth. *J. Atmos. Sci.*, **66**, 3732–3743, doi:10.1175/2009JAS3113.1.
- Shupe, M. D., D. D. Turner, A. Zwink, M. M. Thieman, E. J. Mlawer, and T. Shippert, 2015: Deriving Arctic cloud microphysics at Barrow, Alaska: Algorithms, results, and radiative closure. *J. Appl. Meteor. Climatol.*, **54**, 1675–1689, doi:10.1175/JAMC-D-15-0054.1.
- von Lerber, A. M., D. Moisseev, L. F. Bliven, W. Petersen, A.-M. Harri, and V. Chandrasekar, 2017: Microphysical properties of snow and their link to  $Z_e$ - $S$  relation during BAECC 2014. *J. Appl. Meteor. Climatol.*, **56**, 1561–1581, doi:10.1175/JAMC-D-16-0379.1.